Shell-crossing in a Λ CDM Universe

Cornelius Rampf, Oliver Hahn

Monthly Notices
of the
ROYAL ASTRONOMICAL SOCIETY

MNRAS **501,** L71–L75 (2021)
Advance Access publication 2020 December 12

doi:10.1093/mnrasl/slaa198

Shell-crossing in a ΛCDM Universe

Cornelius Rampf [1]★† and Oliver Hahn [1,2,3]

[1] *Observatoire de la Côte d'Azur, CNRS, Laboratoire Lagrange, Université Côte d'Azur, Boulevard de l'Observatoire, CS 34229, F-06304 Nice, France*
[2] *Department of Astrophysics, University of Vienna, Türkenschanzstraße 17, A-1180 Vienna, Austria*
[3] *Department of Mathematics, University of Vienna, Oskar-Morgenstern-Platz 1, A-1090 Vienna, Austria*

Accepted 2020 December 8. Received 2020 December 7; in original form 2020 October 30

ABSTRACT

Perturbation theory is an indispensable tool for studying the cosmic large-scale structure, and establishing its limits is therefore of utmost importance. One crucial limitation of perturbation theory is shell-crossing, which is the instance when cold-dark-matter trajectories intersect for the first time. We investigate Lagrangian perturbation theory (LPT) at very high orders in the vicinity of the first shell-crossing for random initial data in a realistic three-dimensional Universe. For this, we have numerically implemented the all-order recursion relations for the matter trajectories, from which the convergence of the LPT series at shell-crossing is established. Convergence studies performed at large orders reveal the nature of the convergence-limiting singularities. These singularities are not the well-known density singularities at shell-crossing but occur at later times when LPT already ceased to provide physically meaningful results.

Key words: cosmology: theory – large-scale structure of Universe – dark matter – dark energy.

1 INTRODUCTION

A given function $\Psi(D)$ that is analytic around $D = 0$ can be locally represented by a convergent Taylor series. In physical applications, the maximal value of the (temporal) variable $D = D_\star$ for which the series converges is frequently unknown, always limited by the nearest singularity(ies) in the complex D-plane (sometimes at $D_\star = \infty$), and can be determined, e.g. by using d'Alembert's ratio test.

Mutatis mutandis, the same applies for the cosmological gravitational dynamics of cold dark matter (CDM), at least when formulated in Lagrangian coordinates. Indeed, CDM trajectories can be represented by a convergent Taylor series (Zheligovsky & Frisch 2014; Rampf, Villone & Frisch 2015), however so far only rough estimates on the radius of convergence exist (Michaux et al. 2021). The framework for calculating the Taylor coefficients is called Lagrangian perturbation theory (LPT), with pioneering work done by e.g. Zel'dovich (1970), Buchert (1989), Buchert & Ehlers (1993), Bouchet et al. (1992), Bouchet et al. (1995), and Ehlers & Buchert (1997). None the less, without knowledge of the radius of convergence, spanned by $D_\star$, it is unclear until which time these solutions remain *mathematically* meaningful.

Furthermore, since standard LPT is based on a perfect pressureless fluid description, its predictions are no longer *physically* meaningful once matter trajectories have crossed for the first time. This instance is usually called shell-crossing (sc) and is accompanied by (formally) infinite densities. Shell-crossing is well understood for simplified initial conditions (Novikov 1970; Yano et al. 2004; McQuinn & White 2016; Rampf & Frisch 2017; Taruya & Colombi 2017; Pietroni 2018; Saga, Taruya & Colombi 2018; Rampf 2019; Rampf, Frisch & Hahn 2019), but not so for realistic initial conditions.

Curiously, an infinite density at shell-crossing is not necessarily a convergence-limiting singularity, since in Lagrangian coordinates the density is not a dynamical field but merely a derived quantity. It is the purpose of this work to investigate the rather distinct problems of finding the radius of convergence of LPT, and of detecting the first shell-crossing in a ΛCDM Universe with cosmological constant Λ. We find that LPT converges fairly fast, precisely since the radius of convergence surpasses the instance of the first shell-crossing.

2 SET-UP

We define the peculiar velocity of matter with $\boldsymbol{v} = a\partial_t \boldsymbol{x}$, where $\boldsymbol{x} = \boldsymbol{r}/a$ are comoving coordinates and a is the cosmic scale factor. The basic equations that describe the evolution of matter elements in a ΛCDM Universe are

$$\frac{\mathrm{d}^2\boldsymbol{x}}{\mathrm{d}t^2} + 2H\frac{\mathrm{d}\boldsymbol{x}}{\mathrm{d}t} = -\frac{1}{a^2}\nabla_{\boldsymbol{x}}\phi\,, \qquad \nabla^2_{\boldsymbol{x}}\phi = 4\pi G\bar{\rho}\,a^2\,\delta(\boldsymbol{x})\,, \tag{1}$$

where H is the Hubble parameter, $\bar{\rho}$ the mean matter density of the Universe, and $\delta = (\rho - \bar{\rho})/\bar{\rho}$ the density contrast.

★ E-mail: cornelius.rampf@oca.eu
† Marie Skłodowska-Curie Fellow.

It is standard to solve these equations by introducing the matter trajectory $\boldsymbol{q} \mapsto \boldsymbol{x}(\boldsymbol{q}, t) = \boldsymbol{q} + \boldsymbol{\psi}(\boldsymbol{q}, t)$ from initial position $\boldsymbol{q}$ to current position $\boldsymbol{x}$ at time t, where $\boldsymbol{\psi}(\boldsymbol{q}, t)$ is the Lagrangian displacement field. Until shell-crossing, mass conservation is

$$\delta(\boldsymbol{x}(\boldsymbol{q}, t)) = \frac{1}{J(\boldsymbol{x}(\boldsymbol{q}, t))} - 1\,, \tag{2}$$

where $J = \det(\nabla^{\rm L}\boldsymbol{x})$ is called the Jacobian, and $\nabla^{\rm L}$ denotes a partial derivative in Lagrangian space. The first shell-crossing is achieved for $J(\boldsymbol{q}_{\rm sc}, t_{\rm sc}) \equiv 0$ at the smallest possible time $t_{\rm sc}$ and location $\boldsymbol{q}_{\rm sc}$. As it is well-known, at those locations, we have $\delta \to \infty$.

In standard LPT, equations (1 and 2) are solved with the following *Ansatz* for the displacement $\boldsymbol{\psi} = \boldsymbol{x} - \boldsymbol{q}$:

$$\boldsymbol{\psi}(\boldsymbol{q}, t) = \sum_{n=1}^{\infty} \boldsymbol{\psi}^{(n)}(\boldsymbol{q})\, D^n\,, \tag{3}$$

where $D = D_+(a)$ is the linear growth function in ΛCDM, which we use here as a refined time variable. Taking divergence and curl operations of (1) and matching the powers in D^n, one obtains all-order recurrence relations for the spatial coefficients (Rampf 2012; Zheligovsky & Frisch 2014; Matsubara 2015; Rampf et al. 2015)

$$\nabla^{\rm L}\cdot\boldsymbol{\psi}^{(n)} = -\varphi^{\rm ini}_{,ll}\delta^n_1 + \sum_{0<s<n} \frac{(3-n)/2 - s^2 - (n-s)^2}{(n+3/2)\,(n-1)}\mu_2^{(s,n-s)} + \sum_{n_1+n_2+n_3=n} \frac{(3-n)/2 - n_1^2 - n_2^2 - n_3^2}{(n+3/2)\,(n-1)}\mu_3^{(n_1,n_2,n_3)}, \tag{4a}$$

$$\nabla^{\rm L}\times\boldsymbol{\psi}^{(n)} = \tfrac{1}{2}\textstyle\sum_{0<s<n}\frac{n-2s}{n}\nabla^{\rm L}\psi_k^{(s)}\times\nabla^{\rm L}\psi_k^{(n-s)}\,, \tag{4b}$$

where ‘, l’ denotes a partial derivative with respect to component q_l, summation over repeated indices is assumed, and $\varphi^{\rm ini}$ is the initial gravitational potential provided at $a = 0$ (suitably rescaled); see e.g. Michaux et al. (2021) for details how $\varphi^{\rm ini}$ is obtained. Furthermore, $\mu_2^{(n_1,n_2)} = (1/2)[\psi_{l,l}^{(n_1)}\psi_{m,m}^{(n_2)} - \psi_{l,m}^{(n_1)}\psi_{m,l}^{(n_2)}]$ and $\mu_3^{(n_1,n_2,n_3)} = (1/6)\varepsilon_{ikl}\varepsilon_{jmn}\psi_{i,j}^{(n_1)}\psi_{k,m}^{(n_2)}\psi_{l,n}^{(n_3)}$ are purely spatial kernels of the Jacobian, and ε_{ijk} the Levi–Cività symbol. Note that we ignore sub-dominant, higher-order terms $\propto \Lambda$ in equations (4) since we are here interested in observables at rather high redshifts ($z \gg 5$) where they are vanishingly small; this could be rectified if needed.

As regards to the numerical implementation, the divergence and curl relations (4) define a Helmholtz decomposition from which the displacement field can be determined to arbitrary high precision in perturbation theory. These recursion relations can be translated into an efficient algorithm in Fourier space, which we have implemented in the publicly available software package MUSIC2-MONOFONIC.[1] The numerical code is parallelized (MPI + threads), handles convolutions, and space derivatives by employing fast Fourier transforms, and is fully de-aliased. Regarding the latter, this turns out to be memory intensive due to the appearance of cubic terms in equation (4a) for which the computational domain needs to be temporarily extended by a factor twice as much as the usual Orszag's 3/2 rule (Roberts 2011), requiring eight times the memory. In addition, the $\boldsymbol{\psi}^{(n)}$'s need to be stored temporarily. Thus, the primary limitation of generating the displacement is due to limited working memory.

For the cosmological parameters, we set $\Omega_{\rm m} = 0.302$, $\Omega_{\rm b} = 0.045$, $\Omega_\Lambda = 0.698$, $h = 0.703$, $\sigma_8 = 0.811$, and $n_{\rm s} = 0.961$. If not otherwise stated, we evaluate the fields at $N = 256^3$ grid points with box length $L_{\rm box} = 125\,{\rm Mpc}\,h^{-1}$ for which $k_{\rm Ny} = 6.43h\,{\rm Mpc}^{-1}$ is the Nyquist frequency. LPT results are sensitive to the shape of the initial power spectrum, and to elucidate this, we show results for standard CDM, as well as for a *fictitious* warm dark matter (WDM) model with an unrealistically large mass $m_{\rm wdm} = 0.25\,{\rm keV}$ normalized with respect to σ_8, where we employ the Eisenstein & Hu (1998) transfer functions. Details to the used algorithms and numerical tests are provided in the Supplementary Material A.

[1] Available from https://bitbucket.org/ohahn/monofonic.

3 SHELL-CROSSING AND CONVERGENCE

After having numerically implemented perturbative solutions of the displacement to arbitrarily high order, it is natural to ask whether equation (3) defines a convergent series? And if yes, what are the criteria for its breakdown?

Regarding the former, Zheligovsky & Frisch (2014) and Rampf et al. (2015) determined lower bounds on the radius of convergence, implying that the LPT series is time-analytic and converges at least until some finite time. However, these theoretical methods cannot predict the actual radius of convergence for random initial conditions, for which numerical tests should be employed – as we do below.

Regarding the criteria for its breakdown, it is clear that, *physically*, equation (3) remains only meaningful as long as the flow is (locally) in the single-stream regime. Indeed, once the first shell-crossing has occurred, some regions will be occupied with multiple fluid streams which gravitationally interact with each other. However, standard LPT does not encapsulate the resulting non-trivial accelerations in those multistreaming regions. Instead of incorporating such effects, here we rather raise another, highly nontrivial question: for ΛCDM initial conditions, is the *actual* radius of convergence of the LPT series limited by the first instance of shell-crossing?

To dissect the distinct problems, we first study the convergence at the first shell-crossing. For this, we generate the displacement coefficients at successively higher orders and search for the spatial grid point location $\boldsymbol{q}_{\rm sc}$, where the perturbatively truncated Jacobian

$$J^{\{n\}} \equiv \det\left(\mathbb{1} + \nabla^{\rm L}\sum_{s=1}^{n}\boldsymbol{\psi}^{(s)}(\boldsymbol{q})\,D^s\right) \tag{5}$$

vanishes for the first time ($\mathbb{1}$ is the unit matrix). This search determines $z_{\rm sc}^{(n)}$, which is the nth-order estimate of the redshift of shell-crossing. Then we iterate to higher orders and monitor the trend of $z_{\rm sc}^{(n)}$ at successive orders. In all cases considered, we find that $z_{\rm sc}^{(n)}$ converges to a stable answer, correct to two decimal places, starting at orders between $n = 7$ and 17. Henceforth, we call the converged redshift and corresponding shell-crossing location simply $z_{\rm sc}$ and $\boldsymbol{q}_{\rm sc}$, respectively. Here, the speed of convergence depends mostly on the topology of the seeds that collapse first. See Section 4 for further details, and the Supplementary Material B for explicit case examples as well as sub-grid convergence studies.

Regarding the overall convergence of the Jacobian in the whole spatial domain, in Fig. 1, we show the PDF resulting from taking the difference of perturbatively truncated Jacobians $\Delta J^{\{n\}}(\boldsymbol{q}, z_{\rm sc}) = J^{\{n\}}(\boldsymbol{q}, z_{\rm sc}) - J^{\{n-1\}}(\boldsymbol{q}, z_{\rm sc})$ from all grid points at shell-crossing redshift (here, $z_{\rm sc} = 14.77$ for our base CDM model), for various perturbation orders n. As it is expected for a convergent series, we observe that the truncated distribution of $\Delta J^{\{n\}}$ approaches zero for increasing orders n. Furthermore, the tails in those PDFs lose their support for larger n's: In the specific case shown in the figure, for $n = 5$, 10, and 15, the most extremal absolute deviations of $\Delta J^{\{n\}}$ from 0 are respectively 0.081 44, 0.009 16, and 0.001 57. Actually, even

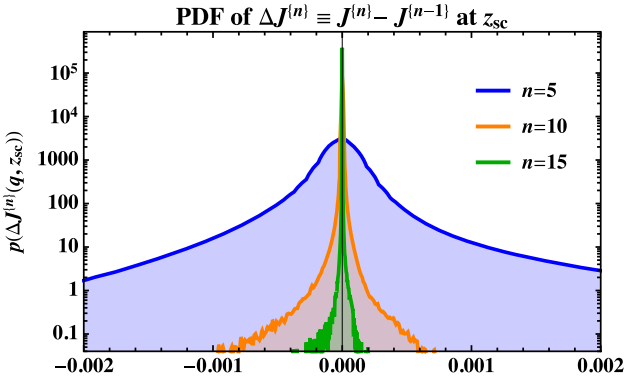

Figure 1. PDF of the residual $\Delta J^{\{n\}}(\boldsymbol{q}) = J^{\{n\}} - J^{\{n-1\}}$ for LPT orders $n = 5$, 10, and 15 (blue, orange, and green lines), evaluated at the redshift of first shell-crossing, which for the present CDM case is at $z_{sc} = 14.77$. This figure demonstrates that LPT displays convergent behaviour at all grid locations.

for those rare events with extremal deviations, which we frequently observed in void regions, LPT displays convergent behaviour until z_{sc} – and even slightly beyond (by employing the Domb–Sykes method explained below). Thus, the Jacobian is converged to at least two decimal places at 10 LPT at shell-crossing time – and not just at $\boldsymbol{q}_{sc}$, but in the whole spatial domain.

We remark that the LPT convergence at z_{sc} can also be observed in Fourier space. For this, we determine the power spectrum P_J of the perturbatively truncated Jacobian at various redshifts, where $\langle \tilde{J}(\boldsymbol{k}_1)\, \tilde{J}(\boldsymbol{k}_2)\rangle = (2\pi)^3 \delta_D^{(3)}(\boldsymbol{k}_1 + \boldsymbol{k}_2)\, P_J(k_1)$, with a tilde denoting the Fourier transform, $\delta_D^{(3)}$ being the Dirac delta, and $k = ||\boldsymbol{k}||$. We find that, until the first shell-crossing, P_J is already converged to sub per cent precision at 3 LPT (cf. Michaux et al. 2021); for details, we refer to the Supplementary Material A (see in particular Fig. A4).

Convergence is lost iff, for some later time and for sufficiently high perturbation orders, different refinement levels of perturbative truncations (e.g. for the Jacobian) begin to diverge. This is illustrated in Fig. 2, where we show ratios of P_J at 15th versus 10th order in LPT for various redshifts, for standard CDM (top panel) and a WDM model (bottom panel). Evidently, the 10th and 15th-order predictions for the Jacobian coincide to an extremely high precision at shell-crossing. Even more, this level of precision is maintained shortly after shell-crossing, denoted with $z_\star$, suggesting that the time of mathematical convergence of LPT surpasses the time of shell-crossing – a conclusion that we have reached for all considered initial data and resolutions. Surpassing $z_\star$, by contrast, generally leads to the loss of convergence which, shortly after $z_\star$, is rather subtle, however amplifies and eventually affects all relevant Fourier scales (see Figs A6 and A7 for late-time results). We remark that, strictly speaking, J refers to the physical Jacobian only until shell-crossing but not later; none the less, even at later times, J remains a good indicator of the loss of mathematical convergence.

To pin down the convergence rigorously, we consider the LPT series of the L^2 norms of displacement coefficients

$$\Psi(\boldsymbol{q}, t) \equiv \sum_{n=1}^{\infty} \left\| \boldsymbol{\psi}^{(n)}(\boldsymbol{q}) \right\| \, D^n \,, \tag{6}$$

and perform numerically the ratio test

$$\lim_{n\to\infty} \left\| \boldsymbol{\psi}^{(n)} \right\| / \left\| \boldsymbol{\psi}^{(n-1)} \right\| = \frac{1}{D_\star} \,, \tag{7}$$

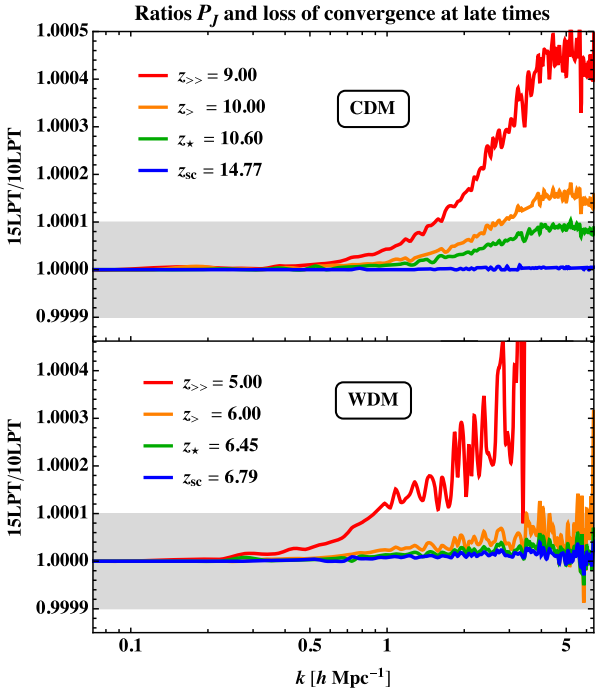

Figure 2. Ratio between power spectra of the truncated Jacobian $J^{\{n\}}$ for $n = 15$ versus $n = 10$ at various redshifts, for CDM (upper panel) and a fictitious WDM model with $m_{wdm} = 0.25$ keV (lower panel). At the redshift of first shell-crossing (z_{sc}), the ratios conform to unity to extremely high precision (grey shading denotes 10^{-4} deviation). Only at much later times, starting at $z_\star$ which marks the estimated redshift of convergence (see Fig. 3), the ratios begin to diverge, thereby revealing the loss of convergence. Evidently, the loss of convergence is rather subtle at those high redshifts, but gets vastly amplified later on (cf. Figs A6 and A7). Note that for results $z \leq z_{sc}$, LPT does not incorporate multistreaming effects.

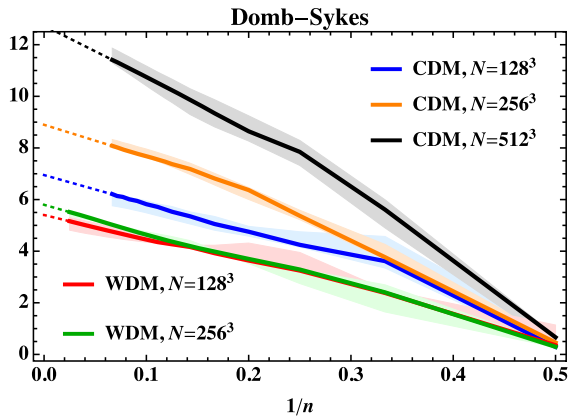

Figure 3. Domb–Sykes plot at first shell-crossing locations $\boldsymbol{q}_{sc}$ for CDM [WDM] up to $n = 15$ [$n = 40$], drawn at various resolutions. Shown are the ratios of subsequent Taylor coefficients $\|\boldsymbol{\psi}^{(n)}\|/\|\boldsymbol{\psi}^{(n-1)}\|$ over $1/n$. For all data, we set $L_{box} = 125\,\mathrm{Mpc}\,h^{-1}$. Lines denote the median obtained from five realizations, shaded regions its 32 and 68 percentiles, while the dotted lines are the respective linear extrapolations at large Taylor orders. The y intercepts of those extrapolations reveal the numerical predictions of the inverse of the radius of convergence (see Table 1).

where $D_\star$ is the radius of convergence (when the limit exists). To do so, we draw in Fig. 3 the Domb–Sykes plot (cf. Domb & Sykes 1957) at the first shell-crossing location, averaged over five realizations.

Table 1. Results from the linear extrapolation $y = m\,(1/n) + b$ of Taylor coefficients $\|\boldsymbol{\psi}^{(n)}\|/\|\boldsymbol{\psi}^{(n-1)}\|$ at large orders n (dotted lines in Fig. 3). The estimated singularity exponent is $\rho = -1 - m/b$, while the convergence redshifts are obtained from $z_\star = 1/a(D)|_{D=D_\star} - 1$, where $D_\star = 1/b$. Finally, $z_{\rm sc}$ denotes here the median of the first shell-crossing redshift, and we have added the 32 and 68 percentiles as errors to $z_\star$ and $z_{\rm sc}$.

Model	N	m	b	ρ	$z_\star$	$z_{\rm sc}$
CDM	128^3	-11.16	6.95	0.61	$7.90^{-0.21}_{-0.81}$	$11.17^{+0.15}_{-0.27}$
CDM	256^3	-12.30	8.90	0.38	$10.40^{+0.21}_{-0.19}$	$15.57^{+0.30}_{-0.80}$
CDM	512^3	-19.90	12.74	0.56	$15.31^{+0.55}_{+0.08}$	$20.69^{+0.27}_{-0.26}$
WDM	128^3	-9.72	5.40	0.80	$5.91^{+0.16}_{-0.54}$	$6.81^{+0.13}_{-0.07}$
WDM	256^3	-11.26	5.80	0.94	$6.42^{+0.06}_{-0.34}$	$6.96^{+0.12}_{-0.12}$

Specifically, for given realization, we draw subsequent ratios of coefficients $\|\boldsymbol{\psi}^{(n)}\|/\|\boldsymbol{\psi}^{(n-1)}\|$ versus $1/n$, and take the y-intercept ('$n \to \infty$') as the estimate for $1/D_\star$ (or, conversely, the redshift of convergence $z_\star$). For WDM, we go up to 40th order in LPT while for CDM we recommend not going beyond $n = 15$ for reasons explained below. The ratios of displacement coefficients settle into a linear behaviour at sufficient high orders, which justifies using a linear extrapolation to the y-intercept (denoted by dotted lines). In Table 1, we show the Medians for $z_\star$ and $z_{\rm sc}$ together with their 32 and 68 percentile variances (for $z_\star$ the variances result from linear extrapolations in the Domb–Sykes plot). For $z_{\rm sc}$, these variances span up the window when shell-crossing is most likely to occur.

Evidently, the value for $z_\star$ is only mildly resolution dependent for WDM, while for CDM the values of $z_\star$ differ substantially. This is due to the non-compact nature of the CDM spectrum, which leads to an intrinsic ultraviolet (UV) dependence at large k. None the less, we expect that this UV dependence should become smaller when the Nyquist frequency is appropriately increased. We leave such computationally challenging avenues for future work.

We note that the linear asymptotic behaviour of Taylor ratios is usually obtained also for single realizations. Only in rare cases, we observe a mild oscillating behaviour superposed on a linear regression: these oscillations appear to arise due to overlapping or adjacent singularities; see Supplementary Material C for details. None the less, even in such cases the ratios of Taylor coefficients still converge to a single point, and thus allow the accurate determination of $z_\star$ – but collude identifying the nature of the singularities.

For the cases when the extrapolation of the Domb–Sykes plot is linear at large orders n, we can assume that the underlying singularities have a pole-like structure with local behaviour

$$\Psi \propto (D - D_\star)^\rho\,, \tag{8}$$

with ρ being a non-integer singularity exponent (if ρ is positive, then derivatives of Ψ blow up). Indeed, as shown by Domb & Sykes (1957), and van Dyke (1974), for such singularities the ratio

$$\|\boldsymbol{\psi}^{(n)}\|/\|\boldsymbol{\psi}^{(n-1)}\| = \frac{1}{D_\star}\left[1 - (1+\rho)\,\frac{1}{n}\right] \tag{9}$$

is exactly linear for large n, which furthermore reveals the large-n asymptotic behaviour $\|\boldsymbol{\psi}^{(n)}\| \simeq \gamma\, n^{-\rho-1}\exp(\beta n)$, with β and γ being fitting coefficients (Podvigina, Zheligovsky & Frisch 2016). See Table 1 for the estimated values of ρ, and the Supplementary Material D for further details. We find that for most cases considered, we have $0 < \rho \lesssim 1$ (and rarely $\rho > 1$), thus indicating that the first-time derivative of the displacement (the velocity) blows up at $D_\star$. We stress again that $D_\star$ is a critical time, which for ΛCDM appears to be always later than the shell-crossing time, i.e. $D_\star > D_{\rm sc}$. Of course, cases when the velocity blows up at $D_\star$ are not physical and just reflect the strength of the underlying singular problem.

Strictly speaking, investigating the singularities in LPT should be done on a case-by-case basis for given random seed, as the outcome of such analysis can depend crucially on the given topology at hand. For example, we find that the singularity exponent is closer to zero if the local initial overdensity has quasi-spherical shape (where LPT converges relatively slowly, cf. Saga et al. 2018; Rampf 2019), while in that case $z_\star$ is just shortly behind $z_{\rm sc}$. By contrast, for initial overdensities that are rather close to being quasi-one-dimensional (where LPT converges fast, see Rampf & Frisch 2017), ρ is larger while $z_\star \ll z_{\rm sc}$; see the Supplementary Material C for specific case examples. None the less, the first shell-crossing usually arises from rather quasi-spherical initial overdensities (see the next section).

Finally, let us comment on why in the CDM case we include 'only' 15th-order effects, while we go up to 40th order for WDM. The $\|\boldsymbol{\psi}^{(n)}(\boldsymbol{q})\|$'s grow exponentially for large orders n at shell-crossing locations, and thus lead to sharp peaks with exponentially increasing height at increasing perturbation order. Since the numerical computations of LPT coefficients involves Fourier transforms, those peaks in $\|\boldsymbol{\psi}^{(n)}(\boldsymbol{q})\|$ can lead to wave-like features in real space due to the Gibbs phenomenon, thereby obscuring the LPT coefficients with unphysical artefacts at very large Taylor orders. These peaks are the sharpest for CDM spectra while they are tamer for WDM spectra, basically since the sharpness of those peaks is related to the information content of the initial density spectra at small spatial scales, where WDM spectra have less support. We find that the Domb–Sykes plot for CDM is unaffected by the Gibbs phenomenon only for $n \lesssim 15$ (see Supplementary Material C for details), while for WDM we could not detect any such limitation. The connection between Fourier series convergence and LPT convergence in these cases could be an interesting aspect of future investigations.

4 WHICH SEEDS/SHAPES COLLAPSE FIRST?

As a last point, we investigate which seeds shell-cross first. In that context, it is useful to consider the Jacobian matrix $\mathbf{J} \equiv \mathbb{1} + \boldsymbol{\nabla}^{\rm L}\boldsymbol{\psi}$ to a given perturbative truncation, and diagonalize its symmetric part into the coordinate system along the fundamental axes. The symmetrized Jacobian, denoted with $J^{\rm s}$, can then be written in terms of the three real eigenvalues $\lambda_{1,2,3} = \lambda_{1,2,3}(\boldsymbol{q}, t)$ as

$$J^{\rm s} = |\,{\rm diag}(\lambda_1, \lambda_2, \lambda_3)\,|\,, \tag{10}$$

where we impose the ordering $\lambda_1 \le \lambda_2 \le \lambda_3$. Locally, shell-crossing is reached when $\lambda_1 \to 0$, while instantaneous multilateral compressions with $\lambda_{1,2} \to 0$, or even $\lambda_{1,2,3} \to 0$, are essentially excluded for random initial conditions (Doroshkevich 1970; Zel'dovich 1970). Note that the above λ_i's relate to the eigenvalues of the so-called deformation tensor $\boldsymbol{\nabla}^{\rm L}\boldsymbol{\psi}$, dubbed $\lambda_{i,{\rm d}}$, according to $\lambda_{i,{\rm d}} = \lambda_i - 1$.

In Fig. 4, we show the resulting distribution of λ_i's at the initial redshift $z_{\rm ini} = 100$ (dashed lines) and shell-crossing redshift $z_{\rm sc}$ (solid lines), obtained for 65 standard ΛCDM random realizations of first shell-crossing locations. To be specific, for a given realization, we search for the first shell-crossing location and evaluate the eigenvalues at those Lagrangian positions at redshift $z_{\rm sc}$ to fifth-order precision, and to second order at $z_{\rm ini} = 100$. Note that $z_{\rm sc}$ varies slightly, depending on the seed, while we keep $z_{\rm ini}$ fixed.

A prominent feature in Fig. 4 is the distribution of λ_1 at $z_{\rm sc}$, which is, as expected, essentially a delta peak at the origin. The other two eigenvalues have medians of 0.41 and 0.65, respectively, indicating that the first collapsing objects have fairly ellipsoidal shape initially. Another noticeable but subtle feature is the appearance of a smaller

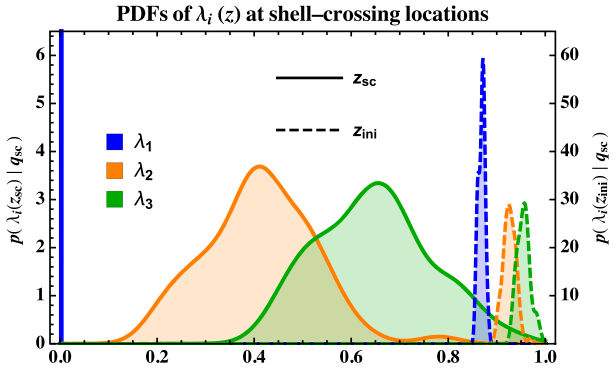

Figure 4. Conditional distribution of eigenvalues of J from locations $\boldsymbol{q} = \boldsymbol{q}_{\rm sc}$ that shell-cross first, obtained from 65 standard-ΛCDM realizations. Shown are the initial distributions at $z_{\rm ini} = 100$ (dashed lines; amplitudes scale according to right y-axis) and at shell-crossing $z_{\rm sc}$ (solid lines; left y-axis).

peak in λ_2 around 0.8 at $z_{\rm sc}$ (that actually traces back to another small peak in $\lambda_2 \simeq 0.96$ at $z_{\rm ini}$), which implies that quasi one-dimensional collapse rarely is the source of the first shell-crossing. The initial distributions of the $\lambda_i(\boldsymbol{q}_{\rm sc}, z_{\rm ini})$'s turn out to be already fairly extreme, with at least 3σ deviations of $\lambda_{2,3}(\boldsymbol{q}_{\rm sc}, z_{\rm ini})$ compared to $\lambda_{2,3}(\boldsymbol{q}, z_{\rm ini})$ from all grid points, and at least 5σ for λ_1.

Finally, we have also investigated the ellipticity $e = (\lambda_{1,\rm d} - \lambda_{3,\rm d})/2\sum\lambda_{i,\rm d}$ and prolateness $p = (\lambda_{1,\rm d} - 2\lambda_{2,\rm d} + \lambda_{3,\rm d})/2\sum\lambda_{i,\rm d}$ of the collapsing seeds in full non-linearity (see Supplementary Material E for linear predictions). For the first shell-crossing locations, we find that both e and p change hardly between $z_{\rm ini}$ and $z_{\rm sc}$, but with a slight tendency in becoming less oblate/prolate at late times. This tendency is also reflected by a slight shift of their medians of $e = 0.171$ and $p = 0.054$ at $z_{\rm ini}$, and $e = 0.168$ and $p = 0.042$ at $z_{\rm sc}$. Further details are provided in the Supplementary Material E.

We remark that the present avenue is fairly distinct from the ones of e.g. Doroshkevich (1970), Bardeen et al. (1986), Sheth, and Mo & Tormen (2001), while those works considered the statistics of peaks by means of linear theory or approximative collapse models, here we investigate the matter collapse on a deterministic and fully non-linear level for various seeds, from which we are able to deduct what the (extreme) statistics of those shell-crossing regions are.

5 CONCLUDING REMARKS

We have shown that LPT can be used to rigorously investigate the first shell-crossing in a ΛCDM Universe. We find that the LPT series for the displacement field converges until shell-crossing and, accidentally, even shortly after. Actually, the latter statement guarantees a rather fast convergence until shell-crossing, thereby allowing to determine time and location of the first shell-crossing efficiently and to high accuracy.

The precise time of first shell-crossing varies with chosen numerical resolution and spectrum of the initial data. In fact, fixing the mesh spacing fixes also an effective fluid description. Below the grid scale, this effective fluid is blind to large-k fluctuations in the spectrum of primordial density fluctuations. Whether such UV effects should be included in cosmic fluid descriptions (and in N-body simulations) is subject to debate (e.g. Taruya, Nishimichi & Jeong 2018; Chen & Pietroni 2020) and should be assessed in forthcoming work.

Our results can be applied to generate accurate initial conditions for numerical N-body simulations, possibly even for simulations with multiple fluids (cf. Hahn, Rampf & Uhlemann 2020; Rampf, Uhlemann & Hahn 2020). Higher-order initial conditions open up the portal for late-time initializations, thereby suppressing strongly discretization errors that affect such simulations at earlier times (see e.g. Michaux et al. 2021). In the long term, our methods assist in closing the gap between theoretical and numerical methods for the cosmic large-scale structure. Possible future directions include the study of LPT against numerical simulation techniques, as well as investigating the fully non-linear formation process of primordial dark-matter haloes within the tidal gravitational field.

ACKNOWLEDGEMENTS

We thank Thomas Buchert, Uriel Frisch, and Patrick McDonald for useful discussions and/or comments on the manuscript. CR acknowledges funding from the People Programme (Marie Curie Actions) of the European Union's Horizon 2020 Programme under grant agreement no. 795707 (COSMO-BLOW-UP). OH acknowledges funding from the European Research Council (ERC) under the European Union's Horizon 2020 research and innovation programme, grant agreement no. 679145 (COSMO-SIMS).

DATA AVAILABILITY

The software implementing nLPT is freely available at https://bitbucket.org/ohahn/monofonic. The data underlying this article will be shared on reasonable request to the corresponding author.

REFERENCES

Bardeen J. M., Bond J. R., Kaiser N., Szalay A. S., 1986, ApJ, 304, 15
Bouchet F. R., Juszkiewicz R., Colombi S., Pellat R., 1992, ApJ, 394, L5
Bouchet F. R., Colombi S., Hivon E., Juszkiewicz R., 1995, A&A, 296, 575
Buchert T., 1989, A&A, 223, 9
Buchert T., Ehlers J., 1993, MNRAS, 264, 375
Chen S.-F., Pietroni M., 2020, J. Cosmol. Astropart. Phys., 06, 033
Domb C., Sykes M. F., 1957, Proc. R. Soc. Lond. A, 240, 214
Doroshkevich A. G., 1970, Astrophysics, 6, 320
Ehlers J., Buchert T., 1997, Gen. Relativ. Gravit., 29, 733
Eisenstein D. J., Hu W., 1998, ApJ, 496, 605
Hahn O., Rampf C., Uhlemann C., 2020, preprint (arXiv:2008.09124)
McQuinn M., White M., 2016, J. Cosmol. Astropart. Phys., 2016, 043
Matsubara T., 2015, Phys. Rev. D, 92, 023534
Michaux M., Hahn O., Rampf C., Angulo R. E., 2021, MNRAS, 500, 663
Novikov E. A., 1970, Sov. Phys. JETP, 30, 512
Pietroni M., 2018, J. Cosmol. Astropart. Phys., 2018, 028
Podvigina O., Zheligovsky V., Frisch U., 2016, J. Comput. Phys., 306, 320
Rampf C., 2012, J. Cosmol. Astropart. Phys., 1212, 004
Rampf C., 2019, MNRAS, 484, 5223
Rampf C., Frisch U., 2017, MNRAS, 471, 671
Rampf C., Villone B., Frisch U., 2015, MNRAS, 452, 1421
Rampf C., Frisch U., Hahn O., 2019, preprint (arXiv:1912.00868)
Rampf C., Uhlemann C., Hahn O., 2020, preprint (arXiv:2008.09123)
Roberts M., 2011, PhD thesis. Univ. Alberta, Edmonton, AB, Canada
Saga S., Taruya A., Colombi S., 2018, Phys. Rev. Lett., 121, 241302
Sheth R. K., Mo H. J., Tormen G., 2001, MNRAS, 323, 1
Taruya A., Colombi S., 2017, MNRAS, 470, 4858
Taruya A., Nishimichi T., Jeong D., 2018, Phys. Rev. D, 98, 103532
van Dyke M., 1974, J. Mech. Appl. Math., 27, 423
Yano T., Koyama H., Buchert T., Gouda N., 2004, ApJS, 151, 185
Zel'dovich Ya. B., 1970, A&A, 500, 13
Zheligovsky V., Frisch U., 2014, J. Fluid Mech., 749, 404

SUPPORTING INFORMATION

Supplementary data are available at *MNRASL* online.
Figure S1. RMS of spurious vorticity.
Figure S2. Power spectrum of Jacobian at various resolution settings.
Figure S3. Resolution dependence of $z_{\rm sc}$.
Figure S4. Power spectrum of Jacobian at various LPT orders at $z_{\rm sc}$.
Figure S5. Norm $||\psi^{(n)}||$ for the first eight orders of nLPT.
Figure S6. Power spectrum of Jacobian at $z = 5$.
Figure S7. Ratio of power spectra of $J^{\{n\}}$ at various redshifts.
Figure S8. Outliers in LPT convergence study.
Figure S9. Conditional distributions of $\lambda_{1,2,3}$ at $z_{\rm sc}$.
Figure S10. PDFs of e and p at the first shell-crossing location.
Figure S11. Scatter plot of $(e,\ p)$ at first shell-crossing locations.
Table S1. Theoretical convergence at shell-crossing locations.
Please note: Oxford University Press is not responsible for the content or functionality of any supporting materials supplied by the authors. Any queries (other than missing material) should be directed to the corresponding author for the article.

This paper has been typeset from a TEX/LATEX file prepared by the author.

List of astronomical key words (Updated on 2020 January)

This list is common to *Monthly Notices of the Royal Astronomical Society, Astronomy and Astrophysics*, and *The Astrophysical Journal*. In order to ease the search, the key words are subdivided into broad categories. No more than *six* subcategories altogether should be listed for a paper.

The subcategories in boldface containing the word 'individual' are intended for use with specific astronomical objects; these should never be used alone, but always in combination with the most common names for the astronomical objects in question. Note that each object counts as one subcategory within the allowed limit of six.

The parts of the key words in italics are for reference only and should be omitted when the keywords are entered on the manuscript.

General
editorials, notices
errata, addenda
extraterrestrial intelligence
history and philosophy of astronomy
miscellaneous
obituaries, biographies
publications, bibliography
sociology of astronomy
standards

Physical data and processes
acceleration of particles
accretion, accretion discs
asteroseismology
astrobiology
astrochemistry
astroparticle physics
atomic data
atomic processes
black hole physics
chaos
conduction
convection
dense matter
diffusion
dynamo
elementary particles
equation of state
gravitation
gravitational lensing: micro
gravitational lensing: strong
gravitational lensing: weak
gravitational waves
hydrodynamics
instabilities
line: formation
line: identification
line: profiles
magnetic fields
magnetic reconnection
(magnetohydrodynamics) MHD
masers
molecular data
molecular processes
neutrinos
nuclear reactions, nucleosynthesis, abundances
opacity
plasmas
polarization
radiation: dynamics
radiation mechanisms:general
radiation mechanisms: non-thermal
radiation mechanisms: thermal
radiative transfer
relativistic processes
scattering
shock waves
solid state: refractory
solid state: volatile
turbulence
waves

Astronomical instrumentation, methods and techniques
atmospheric effects
balloons
instrumentation: adaptive optics
instrumentation: detectors
instrumentation: high angular resolution
instrumentation: interferometers
instrumentation: miscellaneous
instrumentation: photometers
instrumentation: polarimeters
instrumentation: spectrographs
light pollution
methods: analytical
methods: data analysis
methods: laboratory: atomic
methods: laboratory: molecular
methods: laboratory: solid state
methods: miscellaneous
methods: numerical
methods: observational
methods: statistical
site testing
space vehicles
space vehicles: instruments
techniques: high angular resolution
techniques: image processing
techniques: imaging spectroscopy
techniques: interferometric
techniques: miscellaneous
techniques: photometric
techniques: polarimetric
techniques: radar astronomy
techniques: radial velocities
techniques: spectroscopic
telescopes

Astronomical data bases
astronomical data bases: miscellaneous
atlases
catalogues
surveys
virtual observatory tools

Software
software: data analysis
software: development
software: documentation
software: public release
software: simulations

Astrometry and celestial mechanics
astrometry
celestial mechanics
eclipses
ephemerides
occultations
parallaxes
proper motions
reference systems
time

The Sun
Sun: abundances
Sun: activity
Sun: atmosphere
Sun: chromosphere
Sun: corona
Sun: coronal mass ejections (CMEs)
Sun: evolution
Sun: faculae, plages
Sun: filaments, prominences
Sun: flares
Sun: fundamental parameters
Sun: general
Sun: granulation
Sun: helioseismology
Sun: heliosphere
Sun: infrared
Sun: interior
Sun: magnetic fields
Sun: oscillations
Sun: particle emission
Sun: photosphere
Sun: radio radiation
Sun: rotation
(Sun:) solar–terrestrial relations
(Sun:) solar wind
(Sun:) sunspots
Sun: transition region
Sun: UV radiation
Sun: X-rays, gamma-rays

Planetary systems
comets: general

comets: individual: . . .
Earth
interplanetary medium
Kuiper belt: general

Kuiper belt objects: individual: . . .
meteorites, meteors, meteoroids
minor planets, asteroids: general
minor planets, asteroids: individual: . . .
Moon
Oort Cloud
planets and satellites: atmospheres
planets and satellites: aurorae
planets and satellites: composition
planets and satellites: detection
planets and satellites: dynamical evolution and stability
planets and satellites: formation
planets and satellites: fundamental parameters
planets and satellites: gaseous planets
planets and satellites: general

planets and satellites: individual: . . .
planets and satellites: interiors
planets and satellites: magnetic fields
planets and satellites: oceans
planets and satellites: physical evolution
planets and satellites: rings
planets and satellites: surfaces
planets and satellites: tectonics
planets and satellites: terrestrial planets
planet–disc interactions
planet–star interactions
protoplanetary discs
zodiacal dust

Stars
stars: abundances
stars: activity
stars: AGB and post-AGB
stars: atmospheres
(stars:) binaries *(including multiple)*: close
(stars:) binaries: eclipsing
(stars:) binaries: general
(stars:) binaries: spectroscopic
(stars:) binaries: symbiotic
(stars:) binaries: visual
stars: black holes
(stars:) blue stragglers
(stars:) brown dwarfs
stars: carbon
stars: chemically peculiar
stars: chromospheres
(stars:) circumstellar matter
stars: coronae
stars: distances
stars: dwarf novae
stars: early-type
stars: emission-line, Be
stars: evolution
stars: flare
stars: formation
stars: fundamental parameters
(stars:) gamma-ray burst: general
(stars:) **gamma-ray burst: individual: . . .**
stars: general
(stars:) Hertzsprung–Russell and colour–magnitude diagrams
stars: horizontal branch
stars: imaging
stars: individual: . . .
stars: interiors

stars: jets
stars: kinematics and dynamics
stars: late-type
stars: low-mass
stars: luminosity function, mass function
stars: magnetars
stars: magnetic field
stars: massive
stars: mass-loss
stars: neutron
(stars:) novae, cataclysmic variables
stars: oscillations *(including pulsations)*
stars: peculiar *(except chemically peculiar)*
(stars:) planetary systems
stars: Population II
stars: Population III
stars: pre-main-sequence
stars: protostars
(stars:) pulsars: general
(stars:) **pulsars: individual: . . .**
stars: rotation
stars: solar-type
(stars:) starspots
stars: statistics
(stars:) subdwarfs
(stars:) supergiants
(stars:) supernovae: general
(stars:) **supernovae: individual: . . .**
stars: variables: Cepheids
stars: variables: Scuti
stars: variables: general
stars: variables: RR Lyrae
stars: variables: S Doradus
stars: variables: T Tauri, Herbig Ae/Be
(stars:) white dwarfs
stars: winds, outflows
stars: Wolf–Rayet

Interstellar medium (ISM), nebulae
ISM: abundances
ISM: atoms
ISM: bubbles
ISM: clouds
(ISM:) cosmic rays
(ISM:) dust, extinction
ISM: evolution
ISM: general
(ISM:) HII regions
(ISM:) Herbig–Haro objects

ISM: individual objects: . . .
(except planetary nebulae)
ISM: jets and outflows
ISM: kinematics and dynamics
ISM: lines and bands
ISM: magnetic fields
ISM: molecules
(ISM:) photodissociation region (PDR)
(ISM:) planetary nebulae: general
(ISM:) **planetary nebulae: individual: . . .**
ISM: structure
ISM: supernova remnants

The Galaxy
Galaxy: abundances
Galaxy: bulge
Galaxy: centre
Galaxy: disc
Galaxy: evolution
Galaxy: formation
Galaxy: fundamental parameters
Galaxy: general
(Galaxy:) globular clusters: general
(Galaxy:) **globular clusters: individual: . . .**
Galaxy: halo
Galaxy: kinematics and dynamics
(Galaxy:) local interstellar matter
Galaxy: nucleus
(Galaxy:) open clusters and associations: general
(Galaxy:) **open clusters and associations: individual: . . .**
(Galaxy:) solar neighbourhood
Galaxy: stellar content
Galaxy: structure

Galaxies
galaxies: abundances
galaxies: active
galaxies: bar
(galaxies:) BL Lacertae objects: general
(galaxies:) **BL Lacertae objects: individual: . . .**
galaxies: bulges
galaxies: clusters: general

galaxies: clusters: individual: . . .
galaxies: clusters: intracluster medium
galaxies: disc
galaxies: distances and redshifts
galaxies: dwarf
galaxies: elliptical and lenticular, cD
galaxies: evolution
galaxies: formation
galaxies: fundamental parameters
galaxies: general
galaxies: groups: general

galaxies: groups: individual: . . .
galaxies: haloes
galaxies: high-redshift

galaxies: individual: . . .
galaxies: interactions
(galaxies:) intergalactic medium
galaxies: irregular
galaxies: ISM
galaxies: jets
galaxies: kinematics and dynamics
(galaxies:) Local Group
galaxies: luminosity function, mass function
(galaxies:) Magellanic Clouds
galaxies: magnetic fields
galaxies: nuclei
galaxies: peculiar
galaxies: photometry
(galaxies:) quasars: absorption lines
(galaxies:) quasars: emission lines
(galaxies:) quasars: general

(galaxies:) **quasars: individual: . . .**
(galaxies:) quasars: supermassive black holes
galaxies: Seyfert
galaxies: spiral
galaxies: starburst
galaxies: star clusters: general

galaxies: star clusters: individual: . . .
galaxies: star formation
galaxies: statistics
galaxies: stellar content
galaxies: structure

Cosmology
(cosmology:) cosmic background radiation
(cosmology:) cosmological parameters
(cosmology:) dark ages, reionization, first stars
(cosmology:) dark energy
(cosmology:) dark matter
(cosmology:) diffuse radiation
(cosmology:) distance scale
(cosmology:) early Universe
(cosmology:) inflation
(cosmology:) large-scale structure of Universe
cosmology: miscellaneous
cosmology: observations
(cosmology:) primordial nucleosynthesis
cosmology: theory

Resolved and unresolved sources as a function of wavelength
gamma-rays: diffuse background
gamma-rays: galaxies
gamma-rays: galaxies: clusters
gamma-rays: general
gamma-rays: ISM
gamma-rays: stars
infrared: diffuse background
infrared: galaxies
infrared: general
infrared: ISM
infrared: planetary systems
infrared: stars
radio continuum: galaxies
radio continuum: general
radio continuum: ISM
radio continuum: planetary systems
radio continuum: stars
radio continuum: transients
radio lines: galaxies
radio lines: general
radio lines: ISM
radio lines: planetary systems
radio lines: stars
submillimetre: diffuse background
submillimetre: galaxies
submillimetre: general
submillimetre: ISM
submillimetre: planetary systems
submillimetre: stars
ultraviolet: galaxies
ultraviolet: general
ultraviolet: ISM
ultraviolet: planetary systems
ultraviolet: stars
X-rays: binaries
X-rays: bursts
X-rays: diffuse background
X-rays: galaxies
X-rays: galaxies: clusters
X-rays: general
X-rays: individual: . . .
X-rays: ISM
X-rays: stars

Transients
(transients:) black hole mergers
(transients:) black hole - neutron star mergers
(transients:) fast radio bursts
(transients:) gamma-ray bursts
(transients:) neutron star mergers
transients: novae
transients: supernovae
transients: tidal disruption events